Soft Matter

Wetting Behavior of Polyelectrolyte Complex Coacervates on Solid Surfaces

Journal:	*Soft Matter*
Manuscript ID	SM-ART-06-2022-000859.R1
Article Type:	Paper
Date Submitted by the Author:	10-Aug-2022
Complete List of Authors:	Balzer, Christopher; California Institute of Technology, Division of Chemistry and Chemical Engineering Zhang, Pengfei; Donghua University, Center for Advanced Low-dimension Materials Wang, Zhen-Gang; California Institute of Technology Division of Chemistry and Chemical Engineering,

Soft Matter

ARTICLE TYPE

Cite this: DOI: 00.0000/xxxxxxxxxx

Wetting Behavior of Polyelectrolyte Complex Coacervates on Solid Surfaces†

Christopher Balzer,*[a] Pengfei Zhang,[b‡] and Zhen-Gang Wang*[a]

Received Date
Accepted Date

DOI: 00.0000/xxxxxxxxxx

The wetting behavior of complex coacervates underpins their use in many emerging applications of surface science, particularly wet adhesives and coatings. Many factors dictate if a coacervate phase will condense on a solid surface, including solution conditions, the nature of the polymer–substrate interaction, and the underlying supernatant–coacervate bulk phase behavior. In this work, we use a simple inhomogeneous mean-field theory to study the wetting behavior of complex coacervates on solid surfaces both off-coexistence (wetting transitions) and on-coexistence (contact angles). We focus on the effects of salt concentration, the polycation/polyanion surface affinity, and the applied electrostatic potential on the wettability. We find that the coacervate generally wets the surface via a first order wetting transition with second order transitions possible above a surface critical point. Applying an electrostatic potential to a solid surface always improves the surface wettability when the polycation/polyanion–substrate interaction is symmetric. For asymmetric surface affinity, the wettability has a nonmonotonic dependence with the applied potential. We use simple scaling and thermodynamic arguments to explain our results.

1 Introduction

Polyelectrolyte complex coacervation is a type of associative liquid-liquid phase separation where oppositely charged polyelectrolytes separate into a coacervate phase (polymer-rich) and a supernatant phase (polymer-depleted)[1]. In the past few decades, there has been broad interest in complex coacervation due to its wide range of applications across scientific disciplines. For example, complex coacervation has proven to be an efficient means of encapsulation[2], enabling its use in the food[3–6], textile[7–10], and agricultural industries[11]. Emerging technologies of complex coacervates include targeted drug delivery[12,13], fabrication of hydrogels[14], and development of wet adhesives[15].

Utilizing complex coacervation relies on understanding the factors that influence the bulk phase behavior and interfacial properties. Knowing the location of the two-phase boundary for a variety of solution conditions is crucial to exploit the phase transition. There are many factors that contribute to the bulk phase behavior, such as the salt concentration, valency of salt ions, charge state of the polyelectrolytes, chain length, temperature, and sequence of the polymer backbone, which have each been explored with experiments and theory[1,16–18]. In the past decade, there has also been significant progress in characterizing the interfacial properties of the coacervate–supernatant interface — notably, the interfacial tension[19,20]. Experiments and theory of symmetric mixtures of polyelectrolytes have characterized the scaling of interfacial tension with the salt concentration relative to the critical salt concentration[21–29] ($\gamma \sim [\phi_{\pm}^{\mathrm{crit}} - \phi_{\pm}]^{3/2}$) and with the chain length[22,24,30]. Simulations and theory also give access to additional interfacial properties, such interface thickness and excess adsorption[25]. Access to the interfacial profiles is particularly important for asymmetric mixtures of polyelectrolytes, where local charge separation can lead to spatially varying, and usually nonmonotonic, profiles of the electrostatic potential[28,31].

Compared to the coacervate–supernatant interface, the supernatant and coacervate phases near solid surfaces are relatively unexplored. Of central importance for solid substrates is the adsorption and corresponding wetting (or drying) behavior of the coacervate phase. The contact angle (at the substrate-coacervate-supernatant equilibrium) will determine the coacervate's ability to coat a surface. Few works have reported contact angles for these systems, partly due to the difficulty of measuring the contact angle *in situ*[20]. Contact angles are predominantly reported for their relevance to experimental measurements of the interfacial tension, such as colloidal probe atomic force microscopy (CP-AFM) and surface force apparatus (SFA). For example, in measuring interfacial tension with CP-AFM, Spruijt and coworkers pre-

[a] *Division of Chemistry and Chemical Engineering, California Institute of Technology, Pasadena, California 91125, United States. E-mail: balzer@caltech.edu, zgw@caltech.edu*

[b] *State Key Laboratory for Modification of Chemical Fibers and Polymer Materials, Center for Advanced Low-Dimension Materials, College of Material Science and Engineering, Donghua University, Shanghai 201620, China*

† Electronic Supplementary Information (ESI) available. See DOI: 10.1039/cXsm00000x/

sented the contact angle of a coacervate phase in the corresponding supernatant phase on a silica surface for different salt concentrations, reporting contact angles less than 45° and a transition to complete wetting (zero contact angle) above 1 M[21]. Lim *et al.* found that salt solutions in the Hofmeister series at a single salt concentration give contact angles ranging from 25° to above 90° (nonwetting)[32]. In SFA measurements, the interfacial tension is measured via an extrapolation of the pull-off force to zero separation $\gamma = (1/4\pi)(F_{\text{pull},0}/R)\cos\theta$, where R is related to the geometry of the probe. In these measurements, the contact angle has been assumed to be zero (complete wetting) so that $\cos\theta \approx 1$[19,22,33]. Such an assumption dismisses the role of the surface. Overall, the lack of experimental data leaves many open questions. For instance, how do different surface types and solution conditions affect wettability?

Understanding how complex coacervates wet surfaces can inform design of complex coacervates for applications on solid surfaces, like wet adhesives. The performance of wet adhesives critically depends on their ability to wet a substrate in complex and challenging environments, such as the human body[34]. Recently, there has been a proliferation of wet adhesive materials inspired by the adhesives created by marine organisms[15,35], notably the sandcastle worm[36–40] and seawater mussel[33,41–45]. Both of these creatures secrete glue-like proteins that undergo coacervation (complex coacervation or single-component coacervation), wet the adhering surface, and cure into a strong adhesive[46]. Most of the bio-inspired adhesives mimic these glue protein sequences, particularly in their inclusion of 3,4-dihydroxyphenylalanine (DOPA) residues, which serve to both enhance adsorption of the adhesive to the surface and aid in curing the adhesive after oxidation[36,47]. As emphasized by Waite[47], mimicking the residue composition of marine life proteins alone does not capture the complexity of mussel adhesion. The success of mussels in adhering to a variety of surfaces[42] depends on their ability to intricately prepare the surface properties and solution in the proximity of the surface for their adhesive proteins. Replicating the versatility of marine life requires a fundamental understanding of the important factors that influence, and can be used to control, the wetting process.

In this work, we seek to understand and characterize the wetting behavior of symmetric polyelectrolyte complexes near a charged surface. Motivated by the variety of adsorption mechanisms proposed in biological systems[45], we study the effect of salt concentration on the wetting transitions and the contact angle when the polyelectrolyte complexes have nonelectrostatic and/or electrostatic interaction with the surface. To elucidate the main physics in this system, we use a simple inhomogeneous mean-field theory extended from a theory for studying the interfacial behavior of polyelectrolyte complex coacervates developed by Zhang and Wang[28]. The central difference from Ref. 28 is that the polyelectrolyte solution, either coacervate or supernatant, is in contact with a solid surface rather than its coexisting phase. Under the conditions studied, we find that the supernatant to coacervate wetting transition generally occurs via a first order prewetting transition with a second order transition occurring as one approaches the bulk critical salt concentration. Applying an electrostatic potential to the surface shifts the surface critical point away from the bulk critical point and always improves the wettability (lowers contact angles) when polycation and polyanion have identical nonelectrostatic attraction to the surface. However, asymmetry in nonelectrostatic attraction can lead to nonmonotonic changes of the contact angle with the applied potential. Our main finding is that electrostatic manipulation of the substrate is an efficacious method for controlling wettability. Contact angles can be substantially altered by applying small potentials (~ 10 mV), which is a direct result of the low supernatant–coacervate interfacial tension. By studying the effects of electrowetting and nonelectrostatic affinity (i.e. polymer chemistry), this work can serve to guide future design of coacervate materials for applications such as encapsulation, coatings, and adhesives.

2 Theoretical Formulation

To study the wetting behavior, we model a polyelectrolyte solution in contact with a solid surface. Both the model and the theory are similar to that presented by Zhang and Wang[28] so only the main details will be reproduced. The polyelectrolyte solution consists of polycations (p_+), polyanions (p_-), salt ions ($+$ and $-$), and solvent (s), which we describe as coarse-grained beads. The polyanions and polycations have N_{p_+} and N_{p_-} segments where each segment represents a coarse-grained monomer. The monomers and salt ions have valency Z_i, where i is the species. Z_i is positive for positively charged species and negative for negative charges. For the current work, we treat the polyelectrolytes as strong polyelectrolytes where all monomers are fully dissociated and carry the same charge. We treat all species as having the same volume scale of v with a corresponding length scale $\sigma = v^{1/3}$. Further, for simplicity, the counterions dissociated from the polyelectrolytes are assumed to be the same as the corresponding salt ions. Far from the solid surface, the polyelectrolyte solution can be considered uniform with its composition described by the corresponding bulk densities, $\rho^{\text{B}} = \{\rho^{\text{B}}_{p_+}, \rho^{\text{B}}_{p_-}, \rho^{\text{B}}_{+}, \rho^{\text{B}}_{-}, \rho^{\text{B}}_{s}\}$. Here, the polyelectrolyte density $\rho_{p_\pm}$ is the segment (monomer) density. Because the volume scale is the same for all components, it is convenient to work with the volume fractions of each component, and assume incompressibility $\sum_i \phi_i = v\sum_i \rho_i = 1$.

In a homogeneous solution, the Helmholtz free energy density f_{B} can be written as the sum of three different parts, f_{id}, f_{el}, and f_{ch}. These additive free energy terms respectively account for the mixing entropy of the species, electrostatic correlation of a solution of disconnected ions, and the additional electrostatic correlation due to the connectivity of charges along the polyelectrolyte backbone. We do not include any other inter-species interactions like (i.e. Flory–Huggins χ) into the theory in order to focus on the effect of electrostatics; however, these terms can be easily included. The mixing entropy is given by

$$\beta v f_{\text{id}} = \sum_{i=p_+,p_-} \frac{\phi_i}{N_i}\ln(\phi_i) + \sum_{i=+,-}\phi_i \ln(\phi_i) + \left(1 - \sum_{i=p_+,p_-,+,-}\phi_i\right)\ln\left(1 - \sum_{i=p_+,p_-,+,-}\phi_i\right) \quad (1)$$

where $\beta = 1/k_BT$ is defined by the Boltzmann constant k_B and temperature T. The electrostatic correlation is treated at the Debye–Hückel level,

$$\beta v f_{\rm el} = -\frac{1}{4\pi}\left[\ln(1+\kappa\sigma) - \kappa\sigma + \frac{(\kappa\sigma)^2}{2}\right] \quad (2)$$

where κ is the inverse Debye screening length defined as $\kappa\sigma = \sqrt{4\pi(l_{\rm B}/\sigma)\sum_{i=p_\pm,\pm} Z_i^2\phi_i}$. The Bjerrum length has the usual definition of $l_{\rm B} = \beta e^2/4\pi\varepsilon_0\varepsilon_r$, where e is the elementary charge, ε_0 is the vacuum permitivity, and ε_r is the relative dielectric constant of the medium. The first order thermodynamic perturbation theory[48] (TPT1) framework is commonly used to describe the chain connectivity contribution to the electrostatic correlation, but Zhang and Wang recently developed a TPT1-like expression for electrostatic correlation at the Debye–Hückel level that we employ here. We direct readers to Ref. 28 for the full discussion on the derivation. For polyelectrolytes with charge on each segment, the free energy contribution is

$$\beta v f_{\rm ch} = \frac{l_{\rm B}/\sigma}{1+\kappa\sigma}\sum_{i=p_+,p_-}\frac{N_i-1}{N_i}Z_i^2\phi_i \quad (3)$$

With the homogeneous free energy, one can study the bulk phase behavior by calculating the coexisting supernatant–coacervate phase diagram. Since the focus of this work is the role of the solid surface, we provide only a brief description of the supernatant–coacervate phase diagram and direct interested readers to our other works that give a more detailed description[49–51]. For a symmetric polyelectrolyte mixture ($\rho^{\rm B}_{p_+} = \rho^{\rm B}_{p_-}$, $N_{p_+} = N_{p_-}$, $Z_{p_+} = -Z_{p_-}$), as considered in this work, the coexisting concentrations are determined by the equality of chemical potential for each component in the coexisting phases (i.e. $\mu_i^I = \mu_i^{II}$) and equality of osmotic pressure, $\Pi_{\rm B} = \sum_{i=p_\pm,\pm}\mu_i\rho_i - f_{\rm B}$. The set of chemical potentials $\{\mu_i\}_{i=p_\pm,\pm}$ are measured with respect to the chemical potential of the solvent, which can be taken as a constant (zero) due to incompressibility. When the polyelectrolyte mixture is symmetric, the polycation/polyanion and cation/anion concentrations are equal within the same phase. For a given $l_{\rm B}$, there are 4 unknowns ($\rho^I_{p_\pm}$,$\rho^{II}_{p_\pm}$, $\rho^I_\pm$, and $\rho^{II}_\pm$) with 3 independent equations (2 for chemical potential equality and one for osmotic pressure equality). The phase diagram is constructed by specifying one of the unknown components and solving for the other 3 unknowns using a Newton-Raphson approach. By scanning over $\rho^{II}_\pm$, for example, one can construct a phase diagram in the salt–polymer plane.

We extend the homogeneous free energy $f_{\rm B}$ to the inhomogeneous case by using a local approximation of the bulk free energy density and introducing additional mean-field level free energy contributions to account for the inhomogeneous spatial densities. Namely, the Helmholtz free energy for a polyelectrolyte solution in contact with a planar, homogeneous surface is

$$F = A\int_0^\infty dz\Big[f_{\rm B}(\{\rho(z)\}) + \sum_{i=p_+,p_-}\frac{k_BT\ b^2}{6}\left(\frac{d\sqrt{\rho_i(z)}}{dz}\right)^2 + \sum_{i=p_\pm,\pm} eZ_i\rho_i(z)\psi(z) - \frac{\varepsilon_0\varepsilon_r}{2}\left(\frac{d\psi(z)}{dz}\right)^2 + eQ_s\psi(z)\delta(z) + b\sum_{i=p_+,p_-}\eta_i\rho_i(z)\delta(z)\Big] \quad (4)$$

where A is the area of the planar surface, b is the Kuhn length (equivalent to σ in this work), $\psi(z)$ is the mean electrostatic potential, eQ_s is the surface charge density, η is a nonelectrostatic interaction parameter between the polyelectrolyte and solid surface, and $\delta(z)$ is the Dirac delta function. In the expression above, we have assumed that the density variation only takes place in the direction perpendicular to the surface. The first term in Eq. (4) is the free energy density of the homogeneous solution evaluated with the local density. The second term is the Lifshitz entropy that arises from the ground-state dominance approximation in mean-field theory to account for the conformation entropy penalty of the polymer chains due to density inhomogeneity[52]. The third and forth terms are the mean-field energy contributions that arise from local net charge. The final two terms in Eq. (4) account for the solid surface. The term involving Q_s is the surface contribution to the electrostatic free energy that arises from the charge accumulated on the solid surface. The last term accounts for the nonelectrostatic interaction between monomer residues and the surface, which is localized to the surface via the Dirac delta function. We do not include any nonelectrostatic surface interaction for the salt ions in order to focus on the polyelectrolyte adsorption. Treating the polyelectrolyte–substrate interaction this way follows previous studies of neutral polymer[53,54] and polyelectrolyte adsorption[55,56]. Physically, $\eta_{p_\pm}$ does not represent the bare interaction of the monomers with the surface. Instead, $\eta_{p_\pm}$ is a combination of the hard wall repulsion and short range attraction with the surface. As we will see below, a value of zero for $\eta_{p_\pm}$ corresponds to a polyelectrolyte that is indifferent to the surface (neither adsorbing or depleted).

At this point, we emphasize that our theory is a simplified representation of an inhomogeneous system. Treating the electrostatic correlation at the Debye–Hückel level is only valid when electrostatic correlation is relatively weak (i.e. low salt concentration or small surface potentials) and is known to generally overestimate the electrostatic correlation for disconnected beads, while the TPT1 approach underestimates the electrostatic correlation for polyelectrolytes[57]. The majority of works studying complex coacervation have employed a Debye–Hückel electrostatic correlation term with no size correction and no chain connectivity correction, as is the case in VO theory[1]. Currently, there is no widely accepted theory to describe electrostatic correlation in polyelectrolyte solutions, especially for inhomogeneous systems. Additionally, using a local incompressibility assumption only coarsely captures the solvent–monomer or solvent–ion contacts that ex-

ist in real solutions. A hard sphere model may be more realistic but requires commensurate theoretical treatment of electrostatic correlation.

Throughout this work, we will consider systems with a constant electrostatic potential on the surface or constant surface charge density. For a solution in contact with a single surface maintained at constant surface potential ψ_0, the thermodynamic potential that is minimized at equilibrium is

$$\begin{aligned} Y &= F - eQ_sA\psi_0 - \sum_{i=p_\pm,\pm}\mu_i\mathscr{N}_i = \\ &= A\int_0^\infty dz\Big[f_{\mathrm{B}}(\{\rho(z)\}) + \sum_{i=p_\pm,\pm} eZ_i\rho_i(z)\psi(z) - \frac{\varepsilon_0\varepsilon_r}{2}\left(\frac{d\psi(z)}{dz}\right)^2 \\ &\quad + \frac{k_BT\ b^2}{6}\sum_{i=p_+,p_-}\left(\frac{d\sqrt{\rho_i(z)}}{dz}\right)^2 + b\sum_{i=p_+,p_-}\eta_i\rho_i(z)\delta(z) \\ &\quad - \sum_{i=p_\pm,\pm}\mu_i\rho_i(z)\Big] \end{aligned} \quad (5)$$

where $\mathscr{N}_i = A\int_0^\infty \rho_i(z)dz$. Note that the electrostatic surface term is subtracted by the Legendre transform to account for the energy of charging/discharging the surface[58]. For a fixed surface charge density, the relevant free energy is $W = F - \sum_{i=p_\pm,\pm}\mu_i\mathscr{N}_i$. Y and W are equivalent when either Q_s or ψ_0 are zero. We note again that the salt and polyelectrolyte chemical potentials are measured with respect to the pure solvent, which naturally results from the incompressibility condition ($v\sum_{i=p_\pm,\pm,s}\rho_i = 1$). To obtain equilibrium configurations, we extremize the relevant inhomogeneous free energy with respect to the densities and electrostatic potential field to obtain the mean-field equations. Starting with the electrostatic potential, we obtain the Poisson equation

$$\sum_{i=p_\pm,\pm} eZ_i\rho_i(z) + \varepsilon_0\varepsilon_r\frac{d^2\psi}{dz^2} = 0 \quad (6)$$

For the polyelectrolyte densities,

$$\begin{aligned} &\frac{\delta f_{\mathrm{B}}(\{\rho(z)\})}{\delta\rho_{p_\pm}(z)} + b\eta_{p_\pm}\delta(z) - \frac{k_BT\ b^2}{6\sqrt{\rho_{p_\pm}(z)}}\frac{d^2\sqrt{\rho_{p_\pm}(z)}}{dz^2} \\ &\qquad + eZ_{p_\pm}\psi(z) - \mu_{p_\pm} = 0 \end{aligned} \quad (7)$$

For small ions,

$$\frac{\delta f_{\mathrm{B}}(\{\rho(z)\})}{\delta\rho_\pm(z)} + eZ_\pm\psi(z) - \mu_\pm = 0 \quad (8)$$

For fixed surface charge density, the boundary condition for the electrostatic potential is $\varepsilon_0\varepsilon_r\frac{d\psi}{dz}\Big|_{z=0} = -eQ_s$. For fixed surface potential, the boundary condition is simply given by the specified potential at the surface, $\psi(0) = \psi_0$. In either case, far from the surface, the potential can be defined to be zero, $\psi(z\to\infty) = 0$, where we also have $\frac{d\psi}{dz}\Big|_{z\to\infty} = 0$. For the polymer volume fraction, the boundary condition near the surface can be obtained by integrating Eq. (7) from 0^- to 0^+. Only the terms defined at the surface remain, and one obtains

$$\left.\frac{d\sqrt{\rho_{p_\pm}(z)}}{dz}\right|_{z=0} = 6b^{-1}\beta\eta_{p_\pm}\sqrt{\rho_{p_\pm}(0)} \quad (9)$$

As mentioned above, $\eta_{p_\pm}$ is not the bare interaction with the surface but serves as an effective boundary condition for the polymer density. In the absence of a polymer–substrate interaction, the entropic penalty of a polymer chain near a solid surface should lead to depletion[53]. A value of zero for $\eta_{p_\pm}$ indicates the slope of the density profile is zero at the surface, which corresponds to some degree of attraction to overcome the usual depletion arising from loss of conformations near the surface. Likewise, in the absence of electrostatic effects, the sign of $\eta_{p_\pm}$ determines whether the polyelectrolyte is adsorbing or depleted from the surface. These subtleties result from using a continuous chain model (Lifshitz entropy) and have been discussed in detail elsewhere[59]. Far from the surface, the polyelectrolyte volume fractions return to the bulk solution conditions.

We conclude this section by writing the functional form of the surface tension. The surface tension is equal to the excess grand potential energy for constant surface potential system[58]. Subtracting the grand potential energy of the homogeneous system ($Y_0 = -\Pi_{\mathrm{B}}V$) gives

$$\begin{aligned} \gamma = \frac{Y - Y_0}{A} &= \int_0^\infty dz\Big[f_{\mathrm{B}}(\{\rho(z)\}) - f_{\mathrm{B}}(\{\rho^{\mathrm{B}}\}) \\ &\quad + e\sum_{i=p_\pm,\pm} Z_i\rho_i(z)\psi(z) - \frac{\varepsilon_0\varepsilon_r}{2}\left(\frac{d\psi(z)}{dz}\right)^2 \\ &\quad + \frac{k_BTb^2}{6}\sum_{i=p_+,p_-}\left(\frac{d\sqrt{\rho_i(z)}}{dz}\right)^2 - \sum_{i=p_\pm,\pm}\mu_i\Big(\rho_i(z) - \rho_i^{\mathrm{B}}\Big)\Big] \\ &\quad + b\sum_{i=p_+,p_-}\eta_i\rho_i(0) \end{aligned} \quad (10)$$

The expression above can be used to compute either the supernatant–solid or coacervate–solid surface tension. The only difference is the choice of bulk composition. Namely, the choice of $\{\rho^{\mathrm{B}}\}$ will specify whether the bulk solution is on the supernatant or coacervate side of the phase diagram. We note that the surface tension obtained from Eq. 10 is not the true surface tension but the excess surface tension relative to that of a pure solvent. However, the (constant) contribution to the surface tension from the pure solvent has no bearing on the properties of interest in this work (e.g. the contact angle).

2.1 Numerical Considerations

The mean-field equations above are solved by discretizing the spatial coordinate from the surface to a distance far enough from the surface where the volume fraction is sufficiently close to the bulk concentration ($z > 50b$). The set of discretized mean-field equations can be written as $\mathbf{F}(\mathbf{X}) = 0$, where $\mathbf{X} = [\{\phi(z)\},\psi(z)]$. This nonlinear system of equations can be solved in a variety of ways, including relaxation methods or quasi-Newton approaches. We

found that reformulating the problem in terms of fixed-point iterations, where one solves $\mathbf{X} = \mathbf{G}(\mathbf{X}) = \mathbf{X} + \mathbf{F}(\mathbf{X})$, and solving using Anderson Acceleration[60] led to the fastest convergence. The convergence criterion was considered met when the maximum value of $\mathbf{F}(\mathbf{X})$ was less than an error tolerance (10^{-10}).

3 Results and Discussion

We will explore the wetting behavior both off- and on-coexistence. Both refer to locations or trajectories relative to the supernatant–coacervate phase diagram. As the name implies, off-coexistence refers to starting with a system prepared in the one-phase region of the phase diagram and changing a state variable that brings the system closer to the two-phase region. On-coexistence refers to trajectories of the phase diagram that are restricted to the binodal surface, where the contact angle is defined. In this work, in order to reduce the overall number of parameters, we will focus on a single phase diagram constructed in the salt–polyelectrolyte plane. We fix the number of segments for each chain $N_{p_+} = N_{p_-} = N = 100$, the Bjerrum length $l_B/\sigma = 1.785$, and valencies of each species $Z_{p_+} = -Z_{p_-} = Z_+ = -Z_- = 1$ to mimic similar conditions in our earlier work[28]. For $\sigma = 0.4$ nm, the Bjerrum length corresponds to a relative dielectric of $\varepsilon_r \approx 80$ at room temperature.

The resulting supernatant–coacervate phase diagram is shown in Figure 1. Figure 1 shows that the tie-lines connecting the supernatant (dilute) and coacervate (dense) phases are slightly negatively sloped and that above a threshold salt concentration ($\phi_\pm^B = 0.115$), the two phases are indistinguishable. One common feature in the theoretical prediction of bulk phase diagrams of complex coacervates is that the polyelectrolyte concentration in the supernatant phase is exceedingly low[61–66]. In most current theories, including this work, the physical picture of the supernatant phase is a *uniformly mixed* polyelectrolyte solution. In reality, the oppositely charged polyions in the supernatant phase are likely to form dispersed clusters made up of two or more polyions[67–71]. Such a distinction undoubtedly influences the behavior of the supernatant near a solid surface. We recognize this as a limitation of our study; however, using a uniformly mixed assumption allows for the complete phase diagram (Fig. 1), which is useful for mapping surface phase transitions relative to the binodal. The phase diagram near the critical salt concentration is not available when accounting for the polyion clusters in the supernatant phase[70]. Further, we expect many aspects of the wetting behavior to be similar, which we will revisit later on.

The focus of off-coexistence trajectories is whether, and how, the coacervate phase forms on the surface from an unsaturated solution. From Cahn's classical wetting theory[72], reaching coexistence starting from an undersaturated solution generally leads to one of two scenarios. The first is complete wetting, where a macroscopically large, dense film forms on the surface at coexistence. Complete wetting is a surface transition that can be first or second order, depending on whether the film thickness diverges discontinuously or continuously at coexistence, respectively[73]. The second scenario is partial wetting, where the film thickness remains finite at coexistence. To study this, we increase the bulk polymer concentration ($\phi_{p_\pm}^B$) from an undersaturated solution to the saturated solution at a fixed bulk salt concentration, which is a horizontal path (left to right) on the phase diagram in Figure 1. Note that $\phi_\pm^B$ is the overall salt concentration that includes the added salt ions and counterions to the polyelectrolytes so that increasing $\phi_{p_\pm}^B$ for fixed $\phi_\pm^B$ amounts to removing added salt. We calculate the excess adsorption $\Gamma_{ex,i} b^2 = \int_0^\infty \left[\phi_i(x) - \phi_i^B\right] dx$ to measure the presence of the coacervate film.

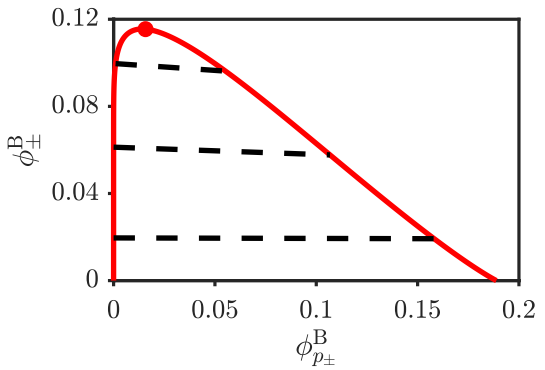

Fig. 1 Supernatant–coacervate bulk phase diagram in the salt–polyelectrolyte plane for $N = 100$ and $l_B/\sigma = 1.785$. Dashed black lines indicate tie-lines. Red point indicates the bulk critical point.

3.1 Nonelectrostatic Wetting

Figure 2 shows adsorption isotherms and interfacial profiles for symmetrically adsorbing polyelectrolytes on a charge-neutral surface for $\phi_\pm^B = 0.1$. Symmetric adsorption means that both polycation and polyanion have identical nonelectrostatic affinity to the surface ($\eta_{p_+} = \eta_{p_-} = \eta_{p_\pm}$). Without an applied potential on the surface or non-zero surface charge density, there is no charge separation so the positive/negative interfacial profiles are identical. The quantity $\Delta\beta\mu_{p_\pm} = \beta\mu_{p_\pm} - \beta\mu_{p_\pm}^{coex}$ measures the chemical potential difference from the chemical potential of the supernatant phase at coexistence. $\Delta\beta\mu_{p_\pm} < 0$ corresponds to an undersaturated supernatant phase in contact with the surface while $\Delta\beta\mu_{p_\pm} < 0$ corresponds to a supersaturated, metastable supernatant phase in contact with the surface. Figure 2a shows the adsorption isotherms for representative values of $\eta_{p_\pm}$. A key feature in this plot is the presence of turning points in the excess adsorption curves. The turning points mark surface spinodals and thus, are an indication of a first order transition. The section of the adsorption isotherm connecting two surface spinodals is thermodynamically unstable. See the ESI† for more detail on turning points and thermodynamic stability.

Surface phase coexistence is determined by the crossing of the relevant surface excess free energy (Figure S2†). For $\beta\eta_{p_\pm} = -0.1$ (purple line in Figure 2a), a first order transition happens near $\Delta\beta\mu_{p_\pm} \approx -0.06$ and then the excess adsorption diverges continuously. A surface transition off-coexistence where the excess adsorption jumps to a finite value is known as a prewetting transition[74], corresponding to coexistence between a thin and thick coacervate layer on the surface[75]. Such a transition is illustrated in the interfacial profiles in Figure 2b. The red and green

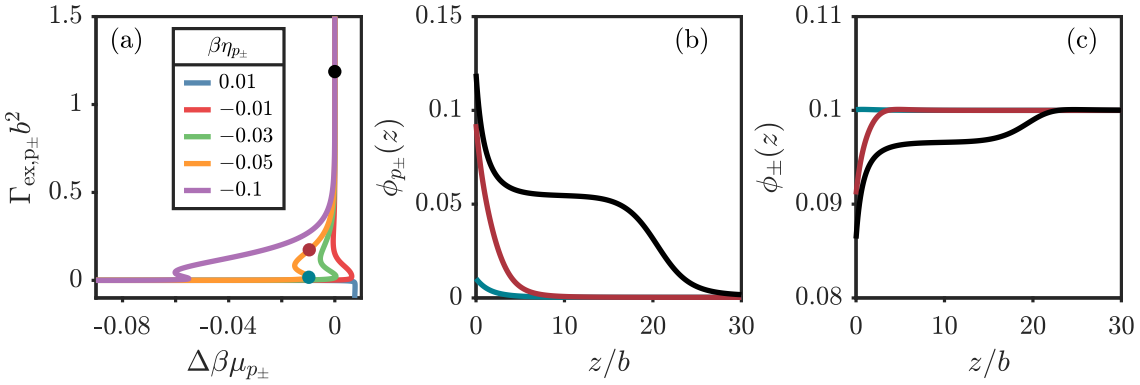

Fig. 2 (a) Polyelectrolyte adsorption isotherms for various nonelectrostatic attraction strengths at a constant bulk salt concentration of $\phi_\pm^{\mathrm{B}} = 0.1$. $\Delta\beta\mu_{p_\pm} = \beta\mu_{p_\pm} - \beta\mu_{p_\pm}^{\mathrm{coex}}$ is a measure of the distance from coexistence. Corresponding (b) polyelectrolyte and (c) salt density profiles before and after the prewetting transition for $\beta\eta_{p_+\pm} = -0.05$. Line colors match the circular markers in (a). For (a), values of $\beta\eta_\pm < -0.01$ undergo complete wetting via a prewetting transition.

lines correspond to coexisting surface phases before and after the transition, respectively. Before the transition (green line), a small amount of polyelectrolyte adsorbs on the surface. After the prewetting transition (red line), there is strong adsorption in the immediate vicinity of the surface, which continuously grows into a macroscopically thick film upon further increase in the bulk concentration (black line). The black curve in Figure 2b reaches a plateau around $z/b = 10$. The same is true in the salt density profiles. As the bulk concentration approaches the binodal, the composition of the plateau approaches the coexisting coacervate phase determined by the phase diagram in Figure 1. The negative tie-lines explain why the coacervate layer depletes salt from the surface. The behavior of the tie-line slope is an active research area[1]. Neitzel and coworkers recently measured positively sloped tie-lines for low charge density polyelectrolytes[76], which would change the trend in salt composition of the wetted coacervate layer.

In Figure 2a, a less favorable polymer–surface interaction shifts or eliminates the prewetting transition. The curve for $\beta\eta_{p_\pm} = -0.01$ exhibits partial wetting. As opposed to the other curves, there is no crossing of the supernatant and coacervate surface excess free energy (Figure S3†). In other words, a coacervate layer on the surface can only exist as metastable state on the supernatant side of the phase diagram for $\beta\eta_{p_\pm} = -0.01$. For $\beta\eta_{p_\pm} = 0.01$, the excess adsorption is actually negative and decreases with bulk concentration, which indicates drying rather than wetting. In that case, the surface also cannot support a coacervate layer. The results presented at this point are similar to that of Monteillet and coworkers that studied coacervation at an oil–water interface using self-consistent field theory[77]. In their work, the formation of a coacervate at the oil-water interface also proceeded via a first order prewetting transition.

By scanning over many salt concentrations, we track the full behavior of the wetting transition. Figure 3 shows the surface phase diagram for $\beta\eta_{p_\pm} = -0.05$ plotted on top of the bulk phase diagram. The green line is the surface spinodal for the supernatant on the surface. Crossing this line from left to right on the diagram results in spontaneous formation of the coacervate layer on the surface (wetting). When the green line falls below the binodal (red), the surface spinodal exists in the metastable region for the bulk supernatant phase. The pink line is the coacervate surface spinodal, where the (metastable) coacervate surface layer must dewet the surface. The black line is the surface coexistence point determined by the crossing point of the relevant free energy (see Figure S2†). Because the surface coexistence line extends off the bulk binodal (red), this line is also known as the prewetting line. As one approaches the critical bulk salt concentration, there is no distinction of supernatant or coacervate phases so the surface transition should be second order in the proximity of the bulk critical point[72]. Indeed, the three lines in the surface phase diagram converge on a surface critical point. Above that point but below the bulk critical point, a horizontal trajectory on the phase diagram leads to a continuous divergence of the excess adsorption, which is consistent with a second order wetting transition. For low salt, the surface coexistence line eventually intersects with the bulk binodal, which we define as the wetting salt concentration, $\phi_\pm^{\mathrm{wet}}$. For the conditions in Figure 3, this occurs at $\phi_\pm^{\mathrm{wet}} \approx 0.053$. One can draw analogy to the wetting temperature typical in liquid-vapor systems[78,79]. The existence of surface spinodals below the wetting salt concentration, called extended wetting, is also expected from classical wetting theory when polyelectrolyte–surface interaction is favorable[80]. When this occurs, the wetted coacervate surface phase can only exist on the surface as a metastable state since there is no crossing of the free energy (see Figure S3†).

When the nonelectrostatic adsorption is asymmetric ($\eta_{p_+} \neq \eta_{p_-}$), the interfacial profiles for the polyions will differ from one another and this charge separation gives rise to a spatially varying electrostatic potential. Figure 4 shows the adsorption isotherms for asymmetric adsorption on a charge-neutral surface ($Q_s = 0$), where we keep $\eta_{p_-} = 0$ while varying the strength of the polycation attraction to the surface η_{p_+}. With $\eta_{p_-} = 0$, polyanions are indifferent to the surface so the formation of the coacervate on the surface must be driven by the adsorption of polycation. Compared to Figure 2, the values of η_{p_+} to induce complete wetting are necessarily higher since polycations must *drag* polyan-

ions to the surface via electrostatic attraction to induce a surface phase transition. The curve for $\beta\eta_{p_+} = -0.1$ in Figure 4 looks qualitatively similar to $\beta\eta_{p_\pm} = -0.05$ in Figure 2a. Another noticeable difference for asymmetric adsorption is the disappearance of turning points for $\beta\eta_{p_+} \leq -0.15$. The excess adsorption diverges continuously, which indicates a second order transition (Figure S4†). Second order wetting transitions are usually associated with systems where long range fluid–fluid interactions are dominant over the short range fluid-solid interaction[81], as is the case near the bulk critical point. The emergence of a second order transition indicates that the electrostatic attraction between adsorbed polycation and indifferent polyanion has an enhanced role in the wetting transition compared to its role in symmetric adsorption, pushing the surface critical point to lower salt concentrations. This result may at first seem nonintuitive since the second order transition develops when the short range polycation–surface interaction (η_{p_+}) becomes *more* favorable. However, increasing η_{p_+} increases the local charge separation near the surface. There must be sufficient charge separation to see the effect of long range electrostatics. At the same salt concentration, for symmetric adsorption, we find only first order transitions when increasing $\beta\eta_{p_\pm}$. The balance of the long range and short range forces is tied to both the strengths and intrinsic length scales of those forces, so we expect nontrivial phenomena to arise from this competition when varying factors like the monomer charge fraction or the salt concentration. Exploring each of these factors is beyond the scope of the current work.

3.2 Electrowetting

Now, we consider the effect of applying an electric potential on the surface transition and surface phase diagram. We consider symmetric adsorption where $\beta\eta_{p_\pm} = -0.05$ with a positive applied surface potential ($\psi_0 > 0$). A positive electrostatic potential will enhance the attraction of the polyanion to the surface and repel the polycation. The adsorption of salt ions will similarly be affected. For a single salt concentration of $\phi^{\mathrm{B}}_{\pm} = 0.1$, we show

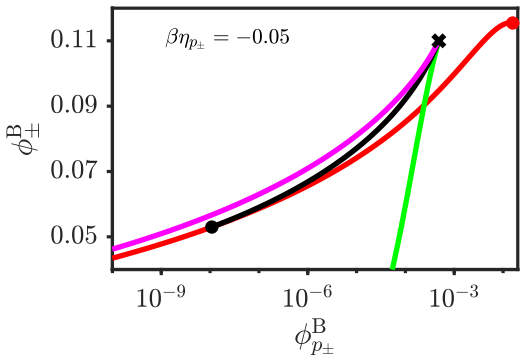

Fig. 3 Surface phase diagram for $\beta\eta_{p_+\pm} = -0.05$ superimposed on bulk phase diagram (red). Lines correspond to supernatant surface spinodal (green), supernatant–coacervate surface coexistence (black), and coacervate surface spinodal (pink). Symbols correspond to the wetting salt concentration (●), the surface critical point (✖), and the bulk critical point (●).

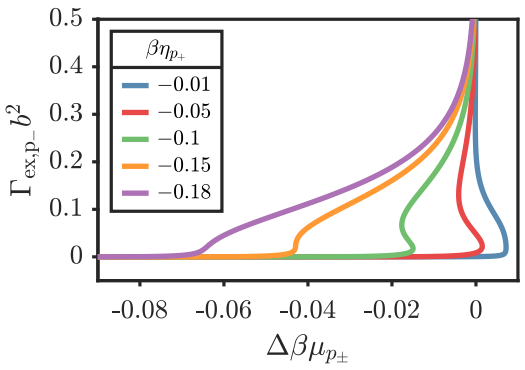

Fig. 4 Polyelectrolyte adsorption isotherms for asymmetric nonelectrostatic attraction strengths ($\eta_{p_+} < 0$ and $\eta_{p_-} = 0$) at a constant bulk salt concentration of $\phi^{\mathrm{B}}_{\pm} = 0.1$. $\Delta\beta\mu_{p_\pm} = \beta\mu_{p_\pm} - \beta\mu^{\mathrm{coex}}_{p_\pm}$ is a measure of the distance from coexistence.

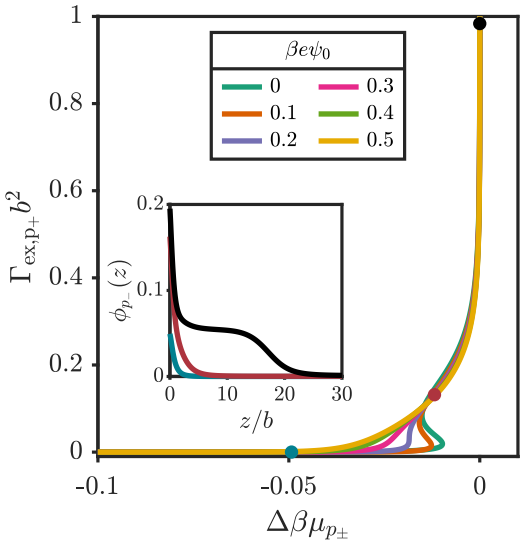

Fig. 5 Polycation adsorption isotherms with $\beta\eta_{p_\pm} = -0.05$ for various surface potentials $\beta e\psi_0$ at a constant bulk salt concentration of $\phi^{\mathrm{B}}_{\pm} = 0.1$. $\Delta\mu_{p_\pm} = \mu_{p_\pm} - \mu^{\mathrm{coex}}_{p_\pm}$ is a measure of the distance from coexistence. (Inset) Polyanion density profiles for $\beta e\psi = 0.3$ corresponding to the matching solid colored points on the adsorption isotherm. For reference, 1 $\beta e\psi \approx$ 22 mV.

the adsorption isotherm of the polycation for various applied potentials in Figure 5. We show the polycation adsorption since the main driving force for its adsorption is the nonelectrostatic interaction with the surface. The polyanion will have higher adsorption for increasing applied potentials to compensate for the positive surface charge density. Figure 5 indicates that as the applied potential increases, the surface transition evolves from a first order prewetting transition to a second order transition. The switch is reflected in the absence of turning points in the curve for $\beta e\psi_0 = 0.5$. This result is similar to the asymmetric nonelectrostatic adsorption discussed previously, where the charge separation enhances the role of long range electrostatic forces.

The inset of Figure 5 shows the polyanion density profiles along the adsorption isotherm for $\beta e\psi_0 = 0.3$. In the region very close

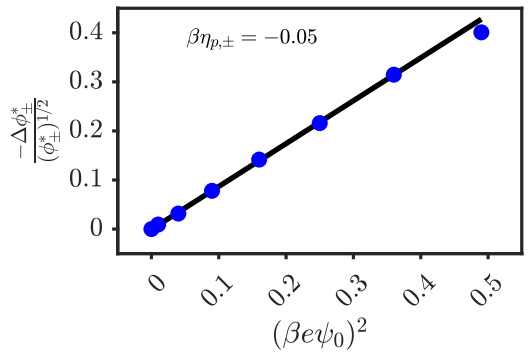

Fig. 6 Rescaled salt concentration of the surface critical point, $\phi_\pm^*$, versus the applied potential for $\beta\eta_{p_\pm} = -0.05$. Rescaled variables are $\Delta\phi_\pm^* = \phi_\pm^* - \left(\phi_\pm^*\right)_{\psi_0=0}$ with $\left(\phi_\pm^*\right)_{\psi_0=0} = 0.11$ (Figure 3). The solid black line indicates the scaling of $-\Delta\phi_\pm^*/\left(\phi_\pm^*\right)^{1/2} \sim \psi_0^2$ fit to the first 3 points predicted points.

to the surface, the adsorption of polyanion is greatly enhanced. Upon approaching the binodal, the coacervate layer grows out of the strongly adsorbing surface layer. The coacervate layer that grows approaches same composition for all values of $\beta e\psi_0$, since, as stated earlier, the eventual composition of the coacervate film is determined by the tie-line on Figure 1. The interfacial profiles for all species, potential profiles, and charge density are shown in Figure S5† for $\beta e\psi_0 = 0.3$. The charge density and potential profile return to bulk values of zero within $z/b = 5$. After this distance, despite the coacervate layer on the surface, the effect of electrostatic adsorption is screened out. Further, Figure S5† shows that the potential profile and charge density crosses zero, which is a sign of strong charge accumulation at the surface and is typical of polyelectrolyte adsorption[82–84]. Practically, these findings are advantageous since one can alter the wetting properties (order of the transition, wetting salt concentration, etc.) by applying a potential without disrupting the coacervate film composition far from the surface. We briefly note that because the non-electrostatic parameters for polycation and polyanion are equal ($\beta\eta_{p_\pm} = -0.05$), applying a negative surface potential rather than a positive one has the same overall effect with the labels for positive/negative species reversed.

The wetting transition is intimately tied to our description of the supernatant phase as uniformly mixed. Figures S5a&b† show that the wetting transition proceeds by initially forming a dense layer of one polyion. We hypothesize that obtaining the same degree of charge separation is unlikely if the supernatant phase is made up of polyion clusters. For this reason, we expect that the assumption of a uniformly mixed supernatant phase overestimates the prevalence of charge separation and thus, the electrostatic effect on the order of the wetting transition. However, we do not currently have a method of describing the adsorption of such polyion clusters to a solid surface.

The crossover from a first order to second order wetting transition in Figure 5 indicates that the salt concentration corresponding to the surface critical point ($\phi_\pm^*$) has moved below $\phi_\pm^B = 0.1$ for applied potentials greater than $\beta e\psi_0 = 0.2$. There are several works that describe how the surface or interfacial tension decreases for small applied potentials (within the linear regime) for solid surfaces[85,86] and even liquid–liquid interfaces[87]. However, the location of the surface critical point does not have an obvious scaling relationship. Using a simple scaling analysis, we hope to give a physical reason for movement of $\phi_\pm^*$. The wetting transition corresponds to replacing the supernatant–solid interface with coacervate–solid and supernatant–coacervate interfaces. Along the prewetting line (black line in Figure 3), the condition for surface phase coexistence is $S = \gamma_{\text{sup,co}} + \gamma_{\text{co,solid}} - \gamma_{\text{sup,solid}} = 0$, where S is the spreading coefficient. Below the bulk critical point, $\gamma_{\text{sup,co}} > 0$ and we can combine the other two terms to represent the effect of adsorption of the coacervate phase compared to the supernatant phase, $F_{\text{ads}}/A = \gamma_{\text{co,solid}} - \gamma_{\text{sup,solid}}$. For favorable adsorption, $F_{\text{ads}}/A < 0$. Thus, the prewetting line is determined by balancing $\gamma_{\text{sup,co}}$ and F_{ads}/A. When applying an electric potential, we consider how $\phi_\pm^*$ should change. We maintain that $S = 0$ so that $\Delta\gamma_{\text{sup,co}} + \Delta F_{\text{ads}}/A = 0$, where the Δ indicates the change from no applied potential ($\psi_0 = 0$). As mentioned in the introduction, the scaling of the interfacial tension with salt concentration is well studied, $\gamma_{\text{sup,co}} \sim (\phi_\pm^{\text{crit}} - \phi^\pm)^{3/2}$. Further, $\Delta F_{\text{ads}}/A$ should scale with the energy stored in the electric double layer, $\Delta F_{\text{ads}}/A \sim -eQ_s\psi_0$. Small applied potentials lead to small changes in $\phi_\pm^*$. Expanding the difference from zero potential to linear order, $\Delta\gamma_{\text{sup,co}} \sim \left(\phi_\pm^*\right)_{\psi_0=0} - \phi_\pm^* \equiv -\Delta\phi_\pm^*$, and for small potentials, $Q_s \sim \kappa\psi_0/l_B$. Assuming the salt concentration is much larger than the polyion concentration at the surface critical point, $\kappa \sim \left(\phi_\pm^*\right)^{1/2}$. Thus, $\Delta F_{\text{ads}}/A \sim -\left(\phi_\pm^*\right)^{1/2}\psi_0^2$ and $\psi_0^2 \sim -\Delta\phi_\pm^*/\left(\phi_\pm^*\right)^{1/2}$. Figure 6 shows this scaling relationship by plotting $-\Delta\phi_\pm^*/\left(\phi_\pm^*\right)^{1/2}$ versus ψ_0^2, where the linear relationship validates the scaling for small applied potential.

3.3 Contact Angle

Finally, we consider wetting behavior on-coexistence. The central quantity in studying on-coexistence wetting is the contact angle. The contact angle stems from the three-phase coexistence between the surface, supernatant, and coacervate phases[78] and is determined from Young's equation.

$$\cos(\theta) = \frac{\gamma_{\text{sup,solid}} - \gamma_{\text{co,solid}}}{\gamma_{\text{sup,co}}} \tag{11}$$

where the terms in the numerator are the supernatant–solid and coacervate–solid surface tension, respectively, and are determined separately from Eq. 10 using bulk conditions from coexisting phases from Figure 1. Although both terms in the numerator should be the total interfacial tension, the contribution from the pure solvent cancels out upon taking the difference, so that only the excess supernatant–solid and coacervate–solid surface tensions are needed. The denominator in Eq. 11 is the interfacial tension, which we calculate using the methods described in our earlier work[28]. Figure S6† gives $\gamma_{\text{sup,co}}$ for the phase diagram in Figure 1. The contact angle is only defined for partially wet sys-

tems. For complete wetting or complete drying, the contact angle will take the values of 0° and 180°, respectively, since one phase will form a macroscopic layer on the surface.

Figure 7 shows the contact angle versus the supernatant salt fraction $(\phi_\pm)^{\text{sup}}$ for symmetric and asymmetric nonelectrostatic adsorption. Starting with the symmetric case, negative values of $\beta\eta_{p_\pm}$ correspond to an favorable (attractive) interaction, while positive values are a repulsive interaction with the surface. Increasing the salt concentration toward the bulk critical salt concentration leads to either complete wetting or complete drying. Complete wetting only occurs for $\eta_{p_\pm} < 0$, which indicates that a favorable nonelectrostatic interaction is required for complete wetting in the absence of electrostatic effects. For $\beta\eta_{p_\pm} = -0.05$, the wetting salt concentration is $(\phi_\pm)^{\text{sup}} \approx 0.053$, which is equivalent to the wetting salt concentration in the surface phase diagram in Figure 3. Increasing the magnitude of the attractive, or repulsive, polyelectrolyte–surface interactions leads to smaller $\phi_\pm^{\text{wet/dry}}$. Figure 7b indicates that complete wetting or drying still occurs when only one component has an interaction with the surface. Compared to the same values of $\beta\eta_{p_+}$ as in Figure 7a, the wetting and drying salt concentrations are higher. Such a result is expected since the driving force for adsorption is not as strong when only one component has an attractive, or repulsive, interaction with the surface.

Qualitatively, the curves featuring complete wetting in Figure 7 resemble data reported by Spruijt and coworkers[21]. To make a direct comparison, we assume a length scale of $\sigma = b = 0.4$ nm and fit $\beta\eta_{p_\pm}$ such that the wetting salt concentration is 1 M, which is consistent with the transition to complete wetting in their work. Figure 8 shows semi-quantitative agreement between the measured and predicted contact angles. We note that we have assumed symmetric adsorption with no electrostatic potential to minimize the number of fitted parameters. While not shown here, one can also achieve similar agreement using the same fitting approach for asymmetric adsorption ($\eta_{p_+} < 0$, $\eta_{p_-} = 0$).

Applying a positive electrostatic potential to the surface increases the favorability of the surface interaction for the polyanion but penalizes adsorption for the polycation. As seen in the shift of the surface critical point for symmetric adsorption, applying a surface potential actually improves the overall wettability (Figure 6). In Figure 9, we show the effect of an applied potential on the contact angle for symmetric adsorption. For no applied potential, complete drying occurs upon increasing the salt concentration. With an applied potential of $\beta e\psi_0 = 0.2$, the system exhibits complete wetting. Further increases in the applied potential move the wetting point lower on the phase diagram. The kink in the contact angle for $\beta e\psi_0 = 0.5$ is due to a prewetting transition that occurs for high applied potentials at low salt concentration (see Figure S7†). The existence of multiple prewetting transitions is well-known for highly favorable adsorption[88]. Physically, these transitions correspond to layering-type transitions, where the strongly adsorbing component (polyanion here) is highly enriched at the surface. We generally find that additional prewetting transitions occur when $\beta e\psi_0 \geq 0.5$ for almost all of the values of $\eta_{p_\pm}$ studied. While we expect our theory to qualitatively identify layering transitions, fully describing layering transitions requires

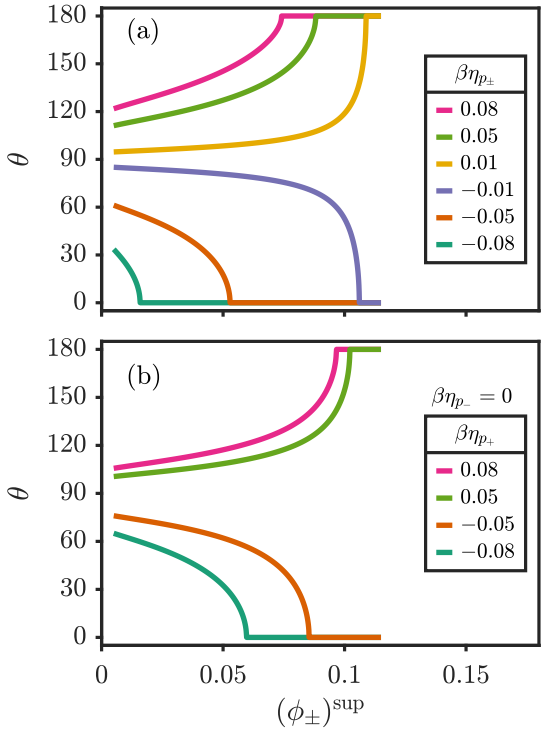

Fig. 7 Contact angle versus supernatant salt fraction for various (a) symmetric adsorption parameters $\beta\eta_{p_\pm}$ and (b) asymmetric adsorption parameters ($\beta\eta_{p_-} = 0$). Critical salt concentration is $\phi_\pm^{\text{crit}} = 0.115$. Contact angles calculated by Eq. 11. In (a) and (b), the electrostatic potential at the surface is zero ($\beta e\psi_0 = 0$). For asymmetric adsorption, the overall potential profile, $\psi(z)$, is non-zero due to the asymmetric interaction with the surface. Coexisting concentrations determined by phase diagram in Figure 1.

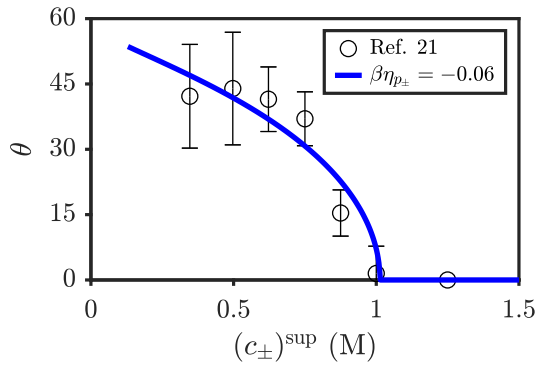

Fig. 8 Contact angle versus salt concentration in the supernatant phase. Line represents symmetric adsorption with a nonelectrostatic adsorption strength $\beta\eta_{p_\pm} = -0.06$, which was determined by fitting described in the text. Experimental data reproduced from Ref. 21 with permission from the Royal Society of Chemistry.

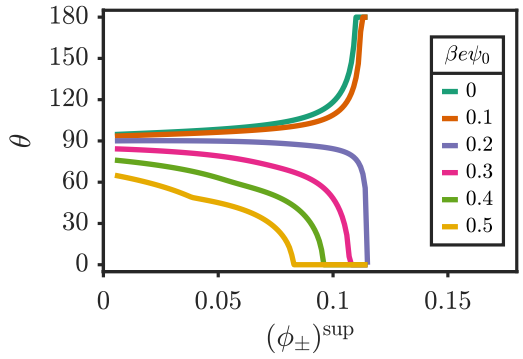

Fig. 9 Contact angle versus the supernatant salt fraction when applying a surface potential for $\beta\eta_\pm = 0.01$. Critical salt concentration is $\phi_\pm^{\text{crit}} = 0.115$. For reference, 1 $\beta e\psi \approx 22$ mV.

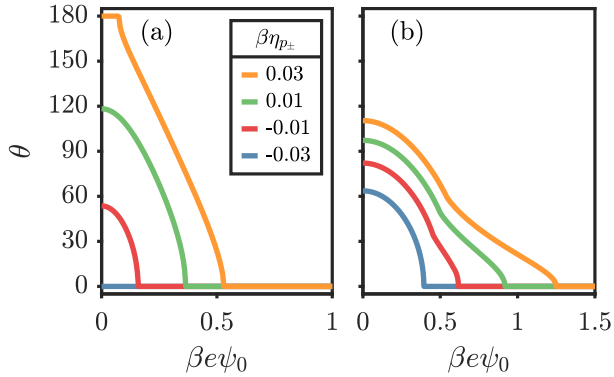

Fig. 10 Contact angle versus applied surface potential for symmetric adsorption at a fixed salt concentration. Bulk salt concentrations are fixed at (a) $\phi_\pm^{\text{B}} = 0.1$ and (b) $\phi_\pm^{\text{B}} = 0.0385$ (1 M). For reference, 1 $\beta e\psi \approx 22$ mV.

a more sophisticated treatment of electrostatic correlation and packing effects, which is beyond the scope of this work.

The observation of layering phenomena seen with applied potentials prompts reevaluation of the underlying physical picture of our theory. At the start of Section 3, we claimed that some aspects of wetting behavior are similar when using the assumption of uniformly mixed polyions compared to explicitly considering polyion clusters in the supernatant phase. In Figure S8†, we compare $\gamma_{\text{sup,solid}}$ from two different representations of the supernatant phase — a solution of uniformly mixed polyelectrolytes and a polyelectrolyte-free solution of salt ions. Both representations have the same osmotic pressure as the coacervate phase. As shown in the ESI†, $\gamma_{\text{sup,solid}}$ is not meaningfully affected by the presence of polyelectrolytes in the supernatant phase, except when there is an applied potential to the surface. In other words, the presence of polyelectrolyte in the supernatant phase does not appreciably influence the contact angle for symmetric and asymmetric nonelectrostatic adsorption without an applied potential. We hypothesize that explicitly considering the nonelectrostatic adsorption of clusters will similarly have little influence on $\gamma_{\text{sup,solid}}$ compared to the $\gamma_{\text{co,solid}}$ so that the contact angles would be unaffected. When applying a surface potential, strong polyelectrolyte adsorption leads to deviations in $\gamma_{\text{sup,solid}}$ from the polyelectrolyte-free case (Figure S8b†). Figure S9† compares the contact angle prediction when using the excess surface tension from the two representations of the supernatant phase. With electrostatic-driven adsorption, we expect polyion clusters would have different adsorption behavior at the coexisting supernatant composition than the uniformly mixed solution. Such differences would be enhanced as the influence of electrostatic effects near the surface increases. We bring these subtleties to the readers' attention to emphasize the limitations and assumptions in our theory. Despite these limitations, we maintain that the essential physics of wetting is captured by the uniformly mixed approach, and we reserve any improved description of adsorption in the supernatant phase to future work.

Figure 10 shows the contact angle as a function of the applied potential for fixed bulk salt concentrations. In either panel, one can see that increasing the applied surface potential decreases the contact angle, eventually leading to complete wetting. Most notably, in Figure 10a, we see that a system with $\beta\eta = 0.03$ initially exhibits complete drying and transitions to complete wetting with an applied potential of less than 15 mV. Lower salt concentrations, like Figure 10b, are further from the critical point so the tendency to wet and dry the surface is lessened. In other words, for all values of $\beta\eta_{p_\pm}$ the contact angle moves toward 90° for $\psi_0 = 0$. Upon applying the potential, all systems transition to complete wetting. However, we again note the kinks in the curves that correspond to additional prewetting transitions. The important aspect from the additional prewetting transition is that the effect of the applied potential is diminished, evidenced by the decrease in the magnitude of the slope of the curves after the kink. For $\beta\eta_{p_\pm} = 0.03$, one can see that the applied potential to induce complete wetting occurs closer to $\beta e\psi_0 = 1.3$, which is nearly double the value in Figure 10a.

We can explain and quantify how the contact angle changes with the applied potential using a simple thermodynamic argument. Consider varying the applied potential for a given supernatant–coacervate tie-line on the phase diagram. Taking the partial derivative of the contact angle with respect to the potential

$$\left(\frac{\partial\cos(\theta)}{\partial\psi_0}\right)_{T,A,\{\mu\}} = \frac{1}{\gamma_{\text{sup,co}}}\left[\left(\frac{\partial\gamma_{\text{sup,solid}}}{\partial\psi_0}\right)_{T,A,\{\mu\}} - \left(\frac{\partial\gamma_{\text{co,solid}}}{\partial\psi_0}\right)_{T,A,\{\mu\}}\right] \quad (12)$$

with $\{\mu\}$ signifying the chemical potentials of all species. The derivatives on the right-hand side are related to the surface charge density by the Maxwell relation[58,89]; thus

$$\left(\frac{\partial\cos(\theta)}{\partial\psi_0}\right)_{T,A,\{\mu\}} = \frac{e\left[(Q_s)^{\text{co}} - (Q_s)^{\text{sup}}\right]}{\gamma_{\text{sup,co}}} \quad (13)$$

where the surface charge densities correspond to that of the coexisting coacervate and supernatant phases each on the solid surface. The second derivative is related to the capacitance of each

phase on the solid surface[85].

$$\left(\frac{\partial^2 \cos(\theta)}{\partial \psi_0^2}\right)_{T,A,\{\mu\}} = \frac{e\left[(C)^{\mathrm{co}} - (C)^{\mathrm{sup}}\right]}{\gamma_{\mathrm{sup,co}}} \tag{14}$$

The capacitance generally increases with concentration so that Eq. 14 is positive. Together, Equations 13 and 14 indicate that $\cos(\theta)$ is minimized when the surface charge of the coacervate and supernatant on the surface is the same. For symmetric adsorption, $(Q_s)^{\mathrm{co}} = (Q_s)^{\mathrm{sup}} = 0$ for no applied potential so that the contact angle will always decrease with an applied potential (positive or negative). Near layering transitions, the capacitance of the supernatant phase can be larger than the coacervate phase for the same potential, resulting from the strong adsorption of one polyion type associated with the transition. This phenomena can been seen as positive curvature in the curves in Figure 10.

Figure 11 shows the wetting/drying salt concentration as a function of the applied potential for various situations. As a reminder, the wetting/drying salt concentration is the salt concentration where the coacervate/supernatant phase completely wets/drys the surface. In Figure 11a, wetting and drying salt concentrations are plotted on the same curve and are differentiated by the line styles. The solid curves denote wetting and the dashed ones indicate drying. One can read each curve as a phase diagram, where vertically crossing the curves from low to high salt concentration corresponds to the transition from partial to complete wetting/drying. We can further interpret an increase in $\phi_{\pm}^{\mathrm{dry}}$ or decrease in $\phi_{\pm}^{\mathrm{wet}}$ as improving the overall wettability below $\phi_{\pm}^{\mathrm{wet/dry}}$. For instance, with $\beta\eta_{p_{\pm}} = 0.01$ (magenta curve), by applying no potential, one can only cross the dashed line, corresponding to complete drying. By applying a negative or positive potential, the drying salt concentration increases, eventually passing through the bulk critical point, indicating the system has switched to complete wetting rather than drying. For the same parameters, this transition from a drying salt concentration to a wetting salt concentration is illustrated in Figure 9. For all of the curves in the symmetric case in Figure 11a, applying a positive or negative potential improves the overall wettability, where drying switches to wetting and/or $\phi_{\pm}^{\mathrm{wet}}$ moves to lower salt concentrations.

For asymmetric adsorption in Figure 11b, we only plot systems that undergo complete wetting. For all parameters considered, the wetting salt concentration has a maximum at positive potentials. This result can best be explained by Equation 13. For no applied potential, polycations adsorb on the surface due to the favorable nonelectrostatic interaction. Polycation adsorption induces a negative surface charge density, and due to the density differences in supernatant and coacervate phases, $(Q_s)^{\mathrm{co}} < (Q_s)^{\mathrm{sup}}$. Because the capacitance of the coacervate is higher than the capacitance of the supernatant $(C)^{\mathrm{co}} > (C)^{\mathrm{sup}}$, applying a positive applied potential will lead to faster changes in $(Q_s)^{\mathrm{co}}$ than $(Q_s)^{\mathrm{sup}}$ so that condition $(Q_s)^{\mathrm{co}} = (Q_s)^{\mathrm{sup}}$ requires a positive applied potential. The net result is a nonmonotonic dependence of the wetting salt concentration on the applied potential. For the conditions in Figure 11b, applying a positive potential initially diminishes the wettability (increases contact angles below $\phi_{\pm}^{\mathrm{wet}}$), then improves wettability after the maximum condition. On the other hand, applying a negative potential will only improve the surface wettability.

4 Conclusions

In this work, we study wetting transitions and contact angles of complex coacervates at solid surfaces. As expected from classical wetting theory, the wettability improves when approaching the bulk critical point. The wetting transition is found to be primarily first order with metastable regions that span multiple orders of magnitude of the polyelectrolyte concentration. Long range electrostatic forces arising from local charge separation can shift the surface critical point to lower salt concentrations, extending the range of second order wetting transitions if there is sufficient nonelectrostatic adsorption asymmetry or an applied surface potential. Many of the results presented here are similar to wetting behavior of simple fluids and polymer blends[90–93]. The essential difference is the presence of electrostatic forces that influence both the phase separation of the polyelectrolytes and possibly their interaction with the surface. The locations of the surface critical point and wetting salt concentration can be tuned by the polymer chemistry (nonelectrostatic interaction) and an applied electrostatic potential on the surface. We rationalize the effect of the electrostatic potential on wettability using arguments from surface thermodynamics.

The issues addressed in this work are relevant to several features seen in nature's underwater adhesives. One aspect is related to symmetric and asymmetric adsorption in biological systems. DOPA residues are prevalent in several of mussel foot proteins[47] compared to the sandcastle worm's adhesive proteins, where DOPA is primarily present in only one of the proteins[36]. Our results indicate that complete wetting is possible when only one component has nonelectrostatic adsorption but such asymmetry generally requires a more favorable polyion–substrate interaction and the wettability is dependent on the electrostatic potential of the surface. As discussed in the introduction, mussels have the ability to tune the surface characteristics. For example, they induce a pH change from 8 (seawater) to less than 5, which will impart a negative zeta potential on most surfaces. As we highlight in our work, electrostatic manipulation of the surface is a powerful method to tune surface wettability, requiring only potential changes on the order of 10 mV to dramatically affect the contact angle. Conversely, given a surface condition (e.g. fixed pH), there are optimal polycation/polyanion characteristics best suited to wet the substrate. Tuning design parameters requires understanding the delicate interplay of nonelectrostatic adsorption with electrostatic-driven adsorption. Overall, we hope that our work can serve as a guide for designing systems that use complex coacervates on solid surfaces.

Recently, the wetting behavior of protein condensates on solid surfaces has also been associated with the origin of life[94]. The general class of surface-mediated processes in biological systems extends beyond solid surfaces. Many of the principles of wetting a solid, rigid surface can be applied to the wetting of soft, elastic substrates[95,96]. Zhao *et al.* used a thermodynamic approach to study how membrane surfaces decorated with surface

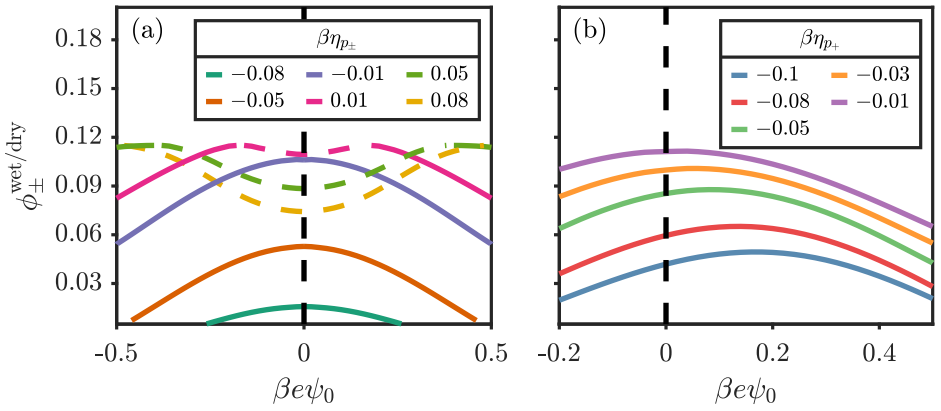

Fig. 11 Wetting/drying salt concentration $\phi_\pm^{\mathrm{wet/dry}}$ versus applied potential for (a) symmetric adsorption and (b) asymmetric adsorption. In (a), dashed lines denote the drying salt concentration, $\phi_\pm^{\mathrm{dry}}$. In both panels, solid lines denote the wetting salt concentration, $\phi_\pm^{\mathrm{wet}}$.

bound molecules improve the wetting of neutral protein condensates[88]. While complex coacervates represent only one type of protein condensate, we expect that extensions of the present work could be used to probe the combined effects of electrostatics and membrane elasticity on the wetting of biological membranes.

We also hope to extend our work to capture some of the physics that our inhomogeneous mean-field theory does not address. As mentioned throughout, treating the supernatant phase as uniformly mixed dismisses the presence of polyion clusters. Forming a coacervate phase on the surface would require the cluster–surface interaction to overcome the translational entropy of the clusters, and in asymmetric adsorption, the energy to rearrange the cluster to facilitate local charge separation[97]. Other important effects not included in this work are strong electrostatic correlation and packing effects near the surface. Substantial adsorption or large applied potentials can lead to layering transitions[75,98,99] and other non-intuitive phenomena[84,100,101] where the Debye–Hückel treatment of electrostatics and a point-particle representation are not expected to be accurate. Capturing each of these effects requires a more sophisticated theory, which remains an outstanding challenge.

Conflicts of Interest

There are no conflicts to declare.

Acknowledgments

C.B. is supported by the U.S. Department of Energy, Office of Science, Office of Advanced Scientific Computing Research, Department of Energy Computational Science Graduate Fellowship under Award Number DE-SC0020347. P.Z. acknowledges the financial support provided by the National Natural Science Foundation of China (NSFC grant nos. 21803011 and 22073016). Z.-G. W. acknowledges financial support from the Hong Kong Quantum AI Lab Ltd.

Notes and references

1 C. E. Sing and S. L. Perry, *Soft Matter*, 2020, **16**, 2885–2914.
2 Y. P. Timilsena, T. O. Akanbi, N. Khalid, B. Adhikari and C. J. Barrow, *International Journal of Biological Macromolecules*, 2019, **121**, 1276–1286.
3 C. Schmitt and S. L. Turgeon, *Advances in Colloid and Interface Science*, 2011, **167**, 63–70.
4 Z. Xiao, W. Liu, G. Zhu, R. Zhou and Y. Niu, *Journal of the Science of Food and Agriculture*, 2014, **94**, 1482–1494.
5 N. Eghbal and R. Choudhary, *LWT - Food Science and Technology*, 2018, **90**, 254–264.
6 Y. P. Timilsena, M. A. Haque and B. Adhikari, *Food and Nutrition Sciences*, 2020, **11**, 481–508.
7 S. Cheng, C. Yuen, C. Kan and K. Cheuk, *Research Journal of Textile and Apparel*, 2008, **12**, 41–51.
8 S. Demirbağ and S. A. Aksoy, *Fibers and Polymers*, 2016, **17**, 408–417.
9 A. López, M. J. Lis, F. M. Bezerra, M. Vilaseca, B. Vallés, R. Prieto and M. Simó, *Journal of Biomedical Science and Engineering*, 2019, **12**, 377–390.
10 D. Massella, S. Giraud, J. Guan, A. Ferri and F. Salaün, *Environmental Chemistry Letters*, 2019, **17**, 1787–1800.
11 Y. Tang, H. B. Scher and T. Jeoh, *Innovative Food Science and Emerging Technologies*, 2020, **59**, 102257.
12 D. J. Burgess, *Macromolecular Complexes in Chemistry and Biology*, Springer Berlin Heidelberg, 1994, pp. 285–300.
13 W. C. Blocher and S. L. Perry, *Wiley Interdisciplinary Reviews: Nanomedicine and Nanobiotechnology*, 2017, **9**, e1442.
14 S. Srivastava, M. Andreev, A. E. Levi, D. J. Goldfeld, J. Mao, W. T. Heller, V. M. Prabhu, J. J. De Pablo and M. V. Tirrell, *Nature Communications*, 2017, **8**, 1–9.
15 G. D. Degen, K. C. Cunha, Z. A. Levine, J. H. Waite and J. E. Shea, *Journal of Physical Chemistry B*, 2021, **125**, 9999–10008.
16 A. Veis, *Advances in Colloid and Interface Science*, 2011, **167**, 2–11.
17 C. E. Sing, *Advances in Colloid and Interface Science*, 2017, **239**, 2–16.
18 A. M. Rumyantsev, N. E. Jackson and J. J. De Pablo, *Annual Review of Condensed Matter Physics*, 2021, **12**, 155–176.

19 Y. S. Jho, H. Y. Yoo, Y. Lin, S. Han and D. S. Hwang, *Advances in Colloid and Interface Science*, 2017, **239**, 61–73.

20 V. M. Prabhu, *Current Opinion in Colloid and Interface Science*, 2021, **53**, 101422.

21 E. Spruijt, J. Sprakel, M. A. Cohen Stuart and J. Van Der Gucht, *Soft Matter*, 2010, **6**, 172–178.

22 D. Priftis, R. Farina and M. Tirrell, *Langmuir*, 2012, **28**, 8721–8729.

23 R. A. Riggleman, R. Kumar and G. H. Fredrickson, *Journal of Chemical Physics*, 2012, **136**, 24903.

24 J. Qin, D. Priftis, R. Farina, S. L. Perry, L. Leon, J. Whitmer, K. Hoffmann, M. Tirrell and J. J. De Pablo, *ACS Macro Letters*, 2014, **3**, 565–568.

25 T. K. Lytle, A. J. Salazar and C. E. Sing, *Journal of Chemical Physics*, 2018, **149**, 163315.

26 A. M. Rumyantsev, E. B. Zhulina and O. V. Borisov, *Macromolecules*, 2018, **51**, 3788–3801.

27 S. Ali and V. M. Prabhu, *Macromolecules*, 2019, **52**, 7495–7502.

28 P. Zhang and Z.-G. Wang, *Macromolecules*, 2021, **54**, 10994–11007.

29 H. Li, M. Fauquignon, M. Haddou, C. Schatz and J. P. Chapel, *Polymers*, 2021, **13**, 3848.

30 D. J. Audus, S. Ali, A. M. Rumyantsev, Y. Ma, J. J. De Pablo and V. M. Prabhu, *Physical Review Letters*, 2021, **126**, 237801.

31 F. Wang, X. Xu and S. Zhao, *Langmuir*, 2019, **35**, 15267–15274.

32 S. Lim, D. Moon, H. J. Kim, J. H. Seo, I. S. Kang and H. J. Cha, *Langmuir*, 2014, **30**, 1108–1115.

33 D. S. Hwang, H. Zeng, A. Srivastava, D. V. Krogstad, M. Tirrell, J. N. Israelachvili and J. H. Waite, *Soft Matter*, 2010, **6**, 3232–3236.

34 Y. Li, J. Cheng, P. Delparastan, H. Wang, S. J. Sigg, K. G. DeFrates, Y. Cao and P. B. Messersmith, *Nature Communications*, 2020, **11**, 1–8.

35 A. Narayanan, A. Dhinojwala and A. Joy, *Chemical Society Reviews*, 2021, **50**, 13321–13345.

36 H. Shao, K. N. Bachus and R. J. Stewart, *Macromolecular Bioscience*, 2009, **9**, 464–471.

37 S. Kaur, G. M. Weerasekare and R. J. Stewart, *ACS Applied Materials and Interfaces*, 2011, **3**, 941–944.

38 L. Zhang, V. Lipik and A. Miserez, *Journal of Materials Chemistry B*, 2016, **4**, 1544–1556.

39 R. J. Stewart, C. S. Wang, I. T. Song and J. P. Jones, *Advances in Colloid and Interface Science*, 2017, **239**, 88–96.

40 M. Vahdati, F. J. Cedano-Serrano, C. Creton and D. Hourdet, *ACS Applied Polymer Materials*, 2020, **2**, 3397–3410.

41 R. J. Stewart, C. S. Wang and H. Shao, *Advances in Colloid and Interface Science*, 2011, **167**, 85–93.

42 Q. Lu, E. Danner, J. H. Waite, J. N. Israelachvili, H. Zeng and D. S. Hwang, *Journal of the Royal Society Interface*, 2013, **10**, 20120759.

43 S. Kim, J. Huang, Y. Lee, S. Dutta, H. Young Yoo, Y. Mee Jung, Y. Jho, H. Zeng and D. S. Hwang, *Proceedings of the National Academy of Sciences of the United States of America*, 2016, **113**, E847–E853.

44 Z. A. Levine, M. V. Rapp, W. Wei, R. G. Mullen, C. Wu, G. H. Zerze, J. Mittal, J. H. Waite, J. N. Israelachvili and J. E. Shea, *Proceedings of the National Academy of Sciences of the United States of America*, 2016, **113**, 4332–4337.

45 Q. Yu, Z. Zheng, X. Dong, R. Cao, S. Zhang, X. Wu and X. Zhang, *Soft Matter*, 2021, **17**, 8786–8804.

46 A. Narayanan, S. Kaur, N. Kumar, M. Tsige, A. Joy and A. Dhinojwala, *Macromolecules*, 2021, **54**, 5417–5428.

47 J. H. Waite, *Journal of Experimental Biology*, 2017, **220**, 517–530.

48 M. S. Wertheim, *The Journal of Chemical Physics*, 1987, **87**, 7323–7331.

49 P. Zhang, N. M. Alsaifi, J. Wu and Z.-G. Wang, *Macromolecules*, 2016, **49**, 9720–9730.

50 P. Zhang, N. M. Alsaifi, J. Wu and Z.-G. Wang, *Journal of Chemical Physics*, 2018, **149**, 163303.

51 A. S. Ylitalo, C. Balzer, P. Zhang and Z.-G. Wang, *Macromolecules*, 2021, **54**, 11326–11337.

52 I. M. Lifshitz, A. Y. Grosberg and A. R. Khokhlov, *Reviews of Modern Physics*, 1978, **50**, 683–713.

53 P. G. de Gennes, *Macromolecules*, 1981, **14**, 1637–1644.

54 A. Johner, J. Bonet-Avaloe, C. C. Van Der Linden, A. N. Semenov and J. F. Joanny, *Macromolecules*, 1996, **29**, 3629–3638.

55 A. Shafir and D. Andelman, *Physical Review E - Statistical Physics, Plasmas, Fluids, and Related Interdisciplinary Topics*, 2004, **70**, 12.

56 Q. Wang, *Macromolecules*, 2005, **38**, 8911–8922.

57 K. Shen and Z.-G. Wang, *Journal of Chemical Physics*, 2017, **146**, 84901.

58 D. Bruch, C. Balzer and Z.-G. Wang, *J. Chem. Phys.*, 2022, **156**, 174704.

59 G. Fredrickson, *The Equilibrium Theory of Inhomogeneous Polymers*, Oxford University Press, New York, 2007, pp. 96–99.

60 H. F. Walker and P. Ni, *SIAM Journal on Numerical Analysis*, 2011, **49**, 1715–1735.

61 J. T. Overbeek and M. J. Voorn, *Journal of Cellular and Comparative Physiology*, 1957, **49**, 7–26.

62 A. Kudlay and M. O. De la Cruz, *Journal of Chemical Physics*, 2004, **120**, 404–412.

63 I. I. Potemkin and V. V. Palyulin, *Physical Review E - Statistical, Nonlinear, and Soft Matter Physics*, 2010, **81**, 041802.

64 J. Qin and J. J. De Pablo, *Macromolecules*, 2016, **49**, 8789–8800.

65 T. K. Lytle and C. E. Sing, *Soft Matter*, 2017, **13**, 7001–7012.

66 P. Zhang, K. Shen, N. M. Alsaifi and Z.-G. Wang, *Macromolecules*, 2018, **51**, 5586–5593.

67 Z. Ou and M. Muthukumar, *Journal of Chemical Physics*, 2006, **124**, 163308.

68 A. M. Rumyantsev and I. I. Potemkin, *Physical Chemistry*

Chemical Physics, 2017, **19**, 27580–27592.
69 A. N. Singh and A. Yethiraj, *Journal of Physical Chemistry B*, 2020, **124**, 1285–1292.
70 P. Zhang and Z.-G. Wang, *Macromolecules*, 2022, **55**, 3910–3923.
71 S. Chen, P. Zhang and Z.-G. Wang, *Macromolecules*, 2022, **55**, 3898–3909.
72 J. W. Cahn, *The Journal of Chemical Physics*, 1977, **66**, 3667–3672.
73 J. Wu, *AIChE Journal*, 2006, **52**, 1169–1193.
74 H. Nakanishi and M. E. Fisher, *Phys. Rev. Lett.*, 1982, **49**, 1565–1568.
75 R. Pandit, M. Schick and M. Wortis, *Physical Review B*, 1982, **26**, 5112–5140.
76 A. E. Neitzel, Y. N. Fang, B. Yu, A. M. Rumyantsev, J. J. De Pablo and M. V. Tirrell, *Macromolecules*, 2021, **54**, 6878–6890.
77 H. Monteillet, J. M. Kleijn, J. Sprakel and F. A. Leermakers, *Advances in Colloid and Interface Science*, 2017, **239**, 17–30.
78 D. Bonn and D. Ross, *Reports on Progress in Physics*, 2001, **64**, 1085–1163.
79 P. Yatsyshin, M. A. Durán-Olivencia and S. Kalliadasis, *Journal of Physics Condensed Matter*, 2018, **30**, 274003.
80 H. Nakanishi and P. Pincus, *The Journal of Chemical Physics*, 1983, **79**, 997–1003.
81 G. F. Teletzke, L. E. Scriven and H. T. Davis, *J. Chem. Phys.*, 1983, **78**, 1431–1439.
82 D. Andelman and J. F. Joanny, *Comptes Rendus de l'Academie des Sciences - Series IV: Physics, Astrophysics*, 2000, **1**, 1153–1162.
83 A. V. Dobrynin, A. Deshkovski and M. Rubinstein, *Macromolecules*, 2001, **34**, 3421–3436.
84 F. Xie, T. Nylander, L. Piculell, S. Utsel, L. Wågberg, T. Åkesson and J. Forsman, *Langmuir*, 2013, **29**, 12421–12431.
85 C. Quilliet and B. Berge, *Current Opinion in Colloid and Interface Science*, 2001, **6**, 34–39.
86 H. Guangze and M. Jianjia, *Continuum Mechanics and Thermodynamics*, 2018, **30**, 817–823.
87 M. Vis, V. F. Peters, E. M. Blokhuis, H. N. Lekkerkerker, B. H. Erné and R. H. Tromp, *Macromolecules*, 2015, **48**, 7335–7345.
88 X. Zhao, G. Bartolucci, A. Honigmann, F. Jülicher and C. A. Weber, *New Journal of Physics*, 2021, **23**, 123003.
89 G. Lippmann, *Ann Chim Phys*, 1875, **5**, 494–549.
90 G. F. Teletzke, L. E. Scriven and H. T. Davis, *The Journal of Chemical Physics*, 1982, **77**, 5794–5798.
91 R. A. Jones, *Polymer*, 1994, **35**, 2160–2166.
92 J. Genzer and R. J. Composto, *Journal of Chemical Physics*, 1997, **106**, 1257–1263.
93 G. G. Pereira, *Journal of Chemical Physics*, 1997, **106**, 4282–4290.
94 İ. Gözen, *Life*, 2021, **11**, 795.
95 J. Agudo-Canalejo, S. W. Schultz, H. Chino, S. M. Migliano, C. Saito, I. Koyama-Honda, H. Stenmark, A. Brech, A. I. May, N. Mizushima and R. L. Knorr, *Nature*, 2021, **591**, 142–146.
96 H. Kusumaatmaja, A. I. May and R. L. Knorr, *Journal of Cell Biology*, 2021, **220**, e202103175.
97 J. v. d. Gucht, E. Spruijt, M. Lemmers and M. A. Cohen Stuart, *Journal of Colloid and Interface Science*, 2011, **361**, 407–422.
98 M. Iwamatsu, *Journal of Colloid and Interface Science*, 1998, **199**, 177–186.
99 A. Oleksy and J. P. Hansen, *Molecular Physics*, 2009, **107**, 2609–2624.
100 W. M. de Vos and S. Lindhoud, *Advances in Colloid and Interface Science*, 2019, **274**, 102040.
101 J. Jiang, *Macromolecules*, 2021, **54**, 1801–1810.